AIAA JOURNAL
Vol. 33, No. 8, August 1995

Numerical Study of Transonic Blade-Vortex Interaction

San-Yih Lin* and Yan-Shin Chin†
National Cheng Kung University, Tainan, Taiwan 70101, Republic of China

Numerical investigations of aerodynamic sound generation due to transonic blade-vortex interaction were performed numerically. The numerical method is based on a third-order upwind finite-volume scheme in space and a second-order explicit Runge–Kutta scheme in time. A standard transonic blade-vortex interaction is presented to demonstrate two dominant sound waves, transonic and compressibility waves. The fluctuation dilatation is presented to identify these two significant sound waves which travel upstream. Three unsteady shock wave motions, types A, B, and C identified by Tijdeman and Seebass, were simulated by changing the physical parameters, such as Mach number, vortex strength, and initial position of the vortex.

Nomenclature

a = vortex core radius
C_p = pressure coefficient
c = sonic speed
e = total energy
M = Mach number
p = static pressure
r = distance between computational point and core of vortex
t = time
u = velocity component in the x-direction
$\boldsymbol{u}$ = velocity vector
$\boldsymbol{v}$ = solenoidal vector
v = velocity component in the y-direction
Γ = vortex strength
γ = ratio of specific heats
Δ = dilatation field
$\bar{\Delta}$ = mean dilatation field
Δ' = fluctuating dilatation field
ρ = density
ϕ = potential function
ϕ' = fluctuating potential field

I. Introduction

THE aerodynamic environment of a helicopter rotor is very complex. It is three dimensional, unsteady, and viscous lowfield, and there exists many possible sources to radiate sound waves. Brooks and Schlinker[1] summarized those noise sources and classified them into discrete and broadband sources. The blade-vortex interaction (BVI) studied here is one of the important discrete sound sources. When a vortex is shed from the rotating blade tip and convected downstream, it intersects with the next rotor blade. The sound source induced from this unsteady vortex motion is called the BVI sound source. If the flow speed increases to transonic speed, the unsteady forces induced from the blade-vortex interaction and shock wave motion induced by the vortex are large and impulsive. The transient changes of the aerodynamic loadings are the most important and dominant source of sound.

Generally, there are two critical BVI conditions classified from the interaction angle between the vortex axis and the blade. The first one is that the blade collides with the vortex normally. In the second, the blade and the vortex axis are parallel. Experimental results of Schlinker and Amiet[2] reveal that the more the blade is parallel to the vortex axis, the more the interaction noise radiates. We concentrate in this research on the two-dimensional, transonic parallel BVI problem. Recently Lent et al.[3] presented two dominant sound waves induced by shock motion in transonic flow. One is called the compressibility wave, and the other is called the transonic wave. According to Lent et al.,[3] when at high subsonic Mach numbers vortices cause an unsteady displacement of the stagnation point at the leading edge of an airfoil and generate a high-pressure region. This high-pressure region then steepens to shock waves. These shock waves will be called compressibility waves. Shock waves due to unsteady and locally confined supersonic flow regions along the shoulder of the airfoil will be called transonic waves. These two sound waves distinguish the transonic noise from those in subsonic flowfields and are studied here.

Three unsteady shock wave motion characteristics have been depicted by Tijdeman and Seebass.[4] The first is sinusoidal shock wave motion (type A). The shock moves periodically and always exists on the airfoil surface only with the variation of position and strength. The second is interrupted shock wave motion (type B). This motion is similar to the motion of type A except that the shock may disappear during its upstream movements. The third is upstream propagating shock waves (type C). The difference between types B and C is that the C-type shock does not disappear during its upstream movements but moves continuously with decreasing strength and finally leaves the leading edge as a free shock wave propagating upstream. Finally, a new shock is formed on the airfoil surface and repeats the upstream movement. Here, we simulated these three motion types in BVI flows by changing the physical parameters, such as Mach number, vortex strength, and position of vortex.

Two-dimensional BVI studies has been numerically performed by many other investigators using potential/Euler/Navier–Stokes solvers.[5–7] Specifically, Lyrintzis et al.[8] has studied the three types (A, B, and C) of shock motion by using a potential solver. Here, we use an Euler solver, modified Osher and Chakravarthy (MOC), scheme developed recently by the present authors[9] to study the transonic BVI flows. The MOC scheme is theoretically third-order accurate in space and second-order in time. This scheme pays special attention to the grid nonuniformity and limiter function so that it remains higher order accurate in nonuniform grids and has low numerical dissipation. The accuracy of the numerical method is assessed by checking grid independence and by comparisons with some analytic and other numerical results. The MOC scheme is described in Sec. II. Two numerical tests are presented in Sec. III. The BVI flowfield visualization will be analyzed in Sec. VI. Acoustic phenomena are discussed in Sec. V, and Sec. VI will consider the shock wave motion.

II. Computational Methods

Flows of two-dimensional, compressible, inviscid, and nonheat conducting fluid can be described in conservation form by the Euler equations

$$W_t + F_x + G_y = 0 \tag{1}$$

Received June 14, 1994; revision received Oct. 11, 1994; accepted for publication Oct. 14, 1994.

*Associate Professor, Institute of Aeronautics and Astronautics. Member AIAA.
†PostDoctor, Institute of Aeronautics and Astronautics.

where

$$W = \begin{pmatrix} \rho \\ \rho u \\ \rho v \\ \rho e \end{pmatrix}, \quad F = \begin{pmatrix} \rho u \\ \rho u^2 + p \\ \rho uv \\ u(\rho e + p) \end{pmatrix}, \quad G = \begin{pmatrix} \rho v \\ \rho uv \\ \rho v^2 + p \\ v(\rho e + p) \end{pmatrix}$$

Here is the total energy per unit mass. The pressure p is given by the equation of state for a perfect gas

$$p = (\gamma - 1)\left[\rho e - \tfrac{1}{2}\rho(u^2 + v^2)\right]$$

where γ (= 1.4 for air) is the ratio of specific heats.

The Euler solver, MOC scheme, solves the two-dimensional, unsteady, Euler equations. This scheme, in strong conservation form, is based on a third-order upwind finite-volume scheme and a second-order explicit Runge–Kutta scheme. A brief description of the implementation of the MOC scheme is demonstrated here for one-dimensional flow. For more details, please see Lin and Chin.[9] Consider the flux F at a surface $i - \frac{1}{2}$, where i is the index of grid in x direction. First, the state of the flow at each interface is described by two vectors of conserved variables on either side, W^L and W^R, as follows:

$$\begin{aligned} W^R_{i-\frac{1}{2}} &= W_i - a_i \cdot \left[(c_i - 2 \cdot \kappa \cdot b_i) \cdot \Delta_{i+\frac{1}{2}} W \right. \\ &\quad \left. + (1/c_i) \cdot (1 + 2 \cdot \kappa \cdot b_i) \cdot \Delta_{i-\frac{1}{2}} W\right] \\ W^L_{i+\frac{1}{2}} &= W_i + a_i \cdot \left[(c_i + 2 \cdot \kappa \cdot b_i) \cdot \Delta_{i+\frac{1}{2}} W \right. \\ &\quad \left. + (1/c_i) \cdot (1 - 2 \cdot \kappa \cdot b_i) \cdot \Delta_{i-\frac{1}{2}} W\right] \end{aligned} \tag{2}$$

where κ is a constant, $-1 \le \kappa \le 1$, and the nonuniformity of cell sizes is taken into account using the parameters a_i, b_i, c_i (Ref. 10). Let ℓ_i represents the width of the ith cell, then

$$\begin{aligned} a_i &= \frac{\ell_i}{\ell_{i+1} + 2 \cdot \ell_i + \ell_{i-1}} \\ b_i &= \frac{\ell_i}{\ell_i + \ell_{i+1}} \\ c_i &= \frac{\ell_i + \ell_{i-1}}{\ell_i + \ell_{i+1}} \end{aligned} \tag{3}$$

Furthermore, to prevent the numerical wiggles around the shock regions, we use the following limiters on W^R and W^L to stabilize the MOC scheme:

$$\begin{aligned} W^{R,(\mathrm{mod})}_{i-\frac{1}{2}} &= W_i - \mathrm{minmod}\left(W_i - W^R_{i-\frac{1}{2}}, \Delta_{i+\frac{1}{2}} W, \Delta_{i-\frac{1}{2}} W\right) \\ W^{L,(\mathrm{mod})}_{i+\frac{1}{2}} &= W_i + \mathrm{minmod}\left(W^L_{i+\frac{1}{2}} - W_i, \Delta_{i+\frac{1}{2}} W, \Delta_{i-\frac{1}{2}} W\right) \end{aligned} \tag{4}$$

The flux at the interface is then obtained by Roe's[11] approximate Riemann solver

$$F_{i-\frac{1}{2}} = \tfrac{1}{2}[F(W^L) + F(W^R) - R|\Lambda|L(W^R - W^L)] \tag{5}$$

where L and R are the left and right eigenmatrices of the Jacobian matrix A at the Roe averaged values of W^R and W^L, and Λ is the corresponding diagonal matrix of eigenvalues. After spatial discretization, a second-order Runge-Kutta scheme is used for the time integration. For the boundary conditions, we use the characteristic boundary condition on the far-field boundary. The solid surface-boundary conditions involve: no penetration for velocity, extrapolation for density, and solving the momentum equation for pressure. Overall, the MOC scheme is formally third-order accurate in space and second-order accurate in time.

Discrete vortices are introduced into the finite-volume computations using a velocity decomposition method.[12] The tangential velocity of the vortex structure is represented by the analytical expression given by[12]

$$\frac{v_\theta}{U_\infty} = \frac{\Gamma}{2\pi r}\left(\frac{r^2}{r^2 + a^2}\right) \tag{6}$$

where a and r are the core radius and the distance from the center of the vortex, respectively; both are nondimensionalized by the chord length of the airfoil. Γ is the vortex strength which is defined by the maximum circulation divided by the freestream velocity and the chord length. The sign of the vortex is positive if it is in a clockwise sense. The pressure and density for the vortex are then obtained by

$$\begin{aligned} \frac{dp}{dr} &= \frac{\rho v_\theta^2}{r} \\ \frac{\gamma p}{(\gamma - 1)\rho} + \frac{v_\theta^2}{2} &= \frac{\gamma p_\infty}{(\gamma - 1)\rho_\infty} \end{aligned} \tag{7}$$

III. Numerical Tests

Two numerical tests are performed here to see the accuracy of the numerical method.

A. Monopole Radiation in a Compressible Stream

First, we consider a uniform stream over a monopole source in an infinite wall.[13] Figure 1 is a schematic of the problem. The volume flow rate of the monopole source is $Q = 10^{-4} \times \sin(2\pi t)$ in a freestream with a Mach number of 0.2. The computational domain covers a finite region of $[-3.5, 3.5] \times [0, 3.5]$ and the monopole source is located at the origin. Three grid systems, 101×50, 151×75, and 281×150 (coarse, mid, and fine) with $(\Delta x, \Delta y)_{\min} = (3.6, 3.6) \times 10^{-2}$, $(2, 2) \times 10^{-2}$, and $(8.9, 7.7) \times 10^{-3}$, respectively, are used. Grids are stretching in both x and y directions (stretching ratio 1.073, 1.02, and 1.013 with respect to coarse, mid, and fine grid). Comparison of the results is done at $t = 5$. Figure 2 shows the pressure at $y = 2.508$ obtained by the MOC scheme. The solid line in this figure presents the exact solution.[13] This figure shows that the computational results are satisfactory. The inaccuracy found in the upwind direction is due to the grid stretching in the x direction.

B. Blade-Vortex Interaction Test

The subsonic blade-vortex interaction problem with a freestream Mach number of 0.536 over a NACA 0012 airfoil at zero angle of attack will serve as the second numerical test. The vortex with $a = 0.164$ and $\Gamma = 0.2481$ is superimposed at $(-5, -0.4)$, i.e., 5 chord lengths from the leading edge of the airfoil and 0.4 chord lengths below the axis of symmetry. Three C-grid systems with meshes of 120×190, 192×190, and 192×270 (coarse, mid, and fine, respectively) are used to test the grid independence. Figure 3

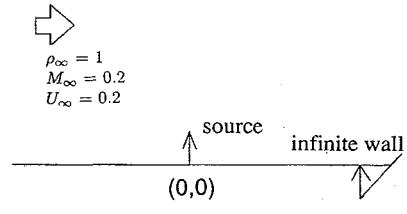

Fig. 1 Schematic of the monopole radiation in a compressible stream.

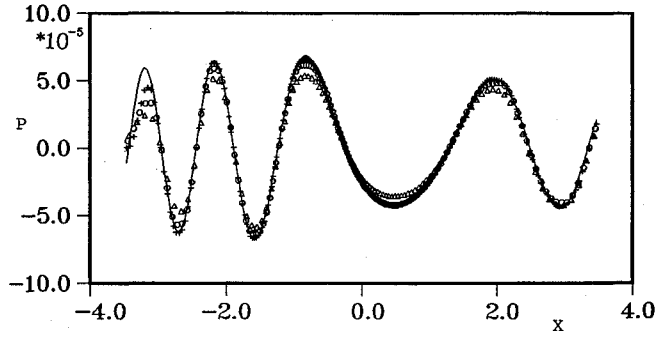

Fig. 2 Pressure plots at $y = 2.508$ obtained by the MOC scheme. Δ coarse, o mid, and + fine grid, respectively.

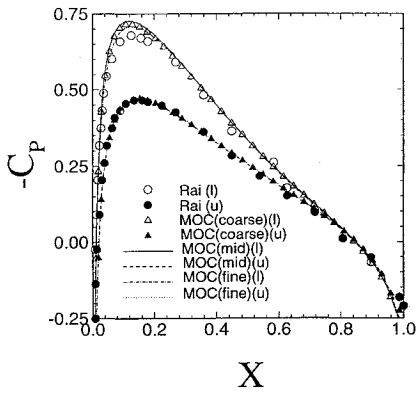

Fig. 3 Surface pressure distributions of the vortex at $(x,y) = (0.289, -0.4)$.

shows the surface pressure distributions as a function of the position of the vortex. The results compare well with Rai's numerical results.[14] One can see that the results obtained by the coarse grid are satisfactory. Therefore, we use the coarse grid to study the blade-vortex interaction problem.

IV. Flowfield Analysis of a Standard Blade-Vortex Interaction Problem

Consider a NACA 0012 airfoil at inflow Mach number $M_\infty = 0.76$. In Eq. 6, the vortex core radius a is set to 0.164 and the vortex strength Γ is set to 0.3. First, the steady-state symmetric flowfield for the flow over the airfoil without the vortex is obtained by using the MOC scheme; then, the vortex is introduced and released from $x_0 = -5$, $y_0 = -0.2$ and convected downstream. At the beginning the vortex is ahead of the leading edge of the airfoil, it induces a downwash on the airfoil which results in the movement of the leading-edge stagnation point. Owing to the effect of the downwash, the stagnation point moves toward the upper surface. The more the stagnation point retreats on the upper surface, the more the flow decelerates on the upper surface. Additionally, continuously slowing down the velocity at the upper surface will weaken the strength of shock and cause the shock to move toward the leading edge and to become even weaker. Finally, the upper surface shock disappears, and the upper surface flowfield is completely subsonic.

As for the lower surface, the situation is different. The flow is accelerated, causing the downstream movement of the location of shock waves, and the shock strength increases. The detailed flow structure and the effect of the vortex can be seen in the pressure contour, Fig. 4. In Fig. 4a, the upper surface shock disappears due to its upstream movement motion, whereas the lower surface shock moves downstream. When the vortex approaches the airfoil, it induces a stronger downwash. After the vortex passes the leading edge, the vortex induces an upwash on the airfoil. Hence, the stagnation point moves back toward the leading edge on the upper surface, and the motion of the stagnation point produces a series of compression waves propagating upstream. Ultimately, those compression waves accumulate to form a shock wave and continuously propagate upstream. Figure 4b shows the compressibility wave indicated by C as defined by Lent et al.[3] Moreover, when the stagnation point moves back, the upper surface flow velocity accelerates and, conversely, the lower surface flow velocity decelerates. Eventually the lower surface shock can not be supported by the pressure difference between the preceding side and the rear side of the shock wave. Consequently the shock wave moves upstream continuously and eventually leaves the leading edge to form a compression wave propagating upstream, as shown in Fig. 4c, where T indicates the transonic wave presented by Lent et al. At the same time, on the upper surface, the flow velocity increases as the pressure is decreasing, and a new shock wave is formed on the upper surface.

Figure 5 shows the vorticity contour. In Fig. 5a, the vorticity is approaching the airfoil. Its structure is clear. At $t = 5.6$, the vortex interacts with the lower shock at around the point $x = 0.6$, $y = -0.2$ as shown in Fig. 5b, and its structure is twisted as compared

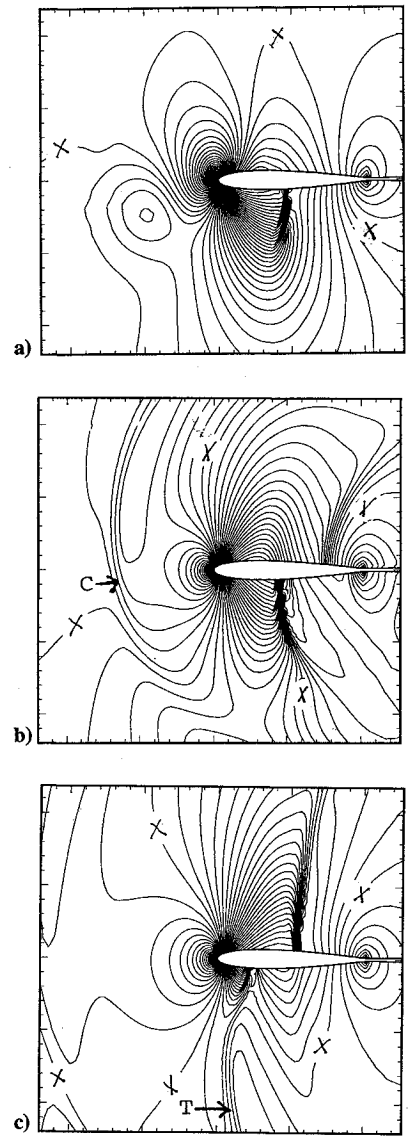

Fig. 4 Instantaneous pressure contours where for BVI at time T = a) 4.6, b) 6.4, and c) 8.0. × indicates pressure $p = p_\infty$.

with the structure of the vortex in Fig. 5a. In Fig. 5c, the vorticity is leaving the airfoil, and its structure is twisted back.

Figure 6 describes the x and y coordinates of the position of the stagnation point as functions of time. At the beginning, the stagnation point moves downstream along the upper surface, and so the y coordinate is positive and the x coordinate is increasing. Then it moves back across the leading edge to the lower surface. Therefore, the y coordinate changes from being positive to negative. When the time is about 8.5, there is a sudden variation of the position of stagnation point. This is caused by the arrival of the propagating transonic wave.

Figure 7 shows the airfoil's upper and lower surface shock wave locations in the x direction. Initially the lower surface shock wave is forced to move downstream. However, as the downstream convecting vortex passes through the leading-edge station, the shock wave moves upstream because of the large pressure difference across the shock wave. Finally, the shock wave leaves the leading edge and propagates upstream as a transonic wave. This is the type C shock wave motion presented by Tijdeman and Seebass.[4] As for the upper surface situation, the shock wave moves upstream with its strength decreasing. Then it disappears from the upper surface. After the traveling vortex has passed through the leading-edge station, a new shock wave is formed gradually and then moves upstream slowly with the departure of the traveling vortex behind the airfoil. This is type B shock wave motion. With regard to the characteristics of the vortex inducing shock wave motion, we will discuss these by

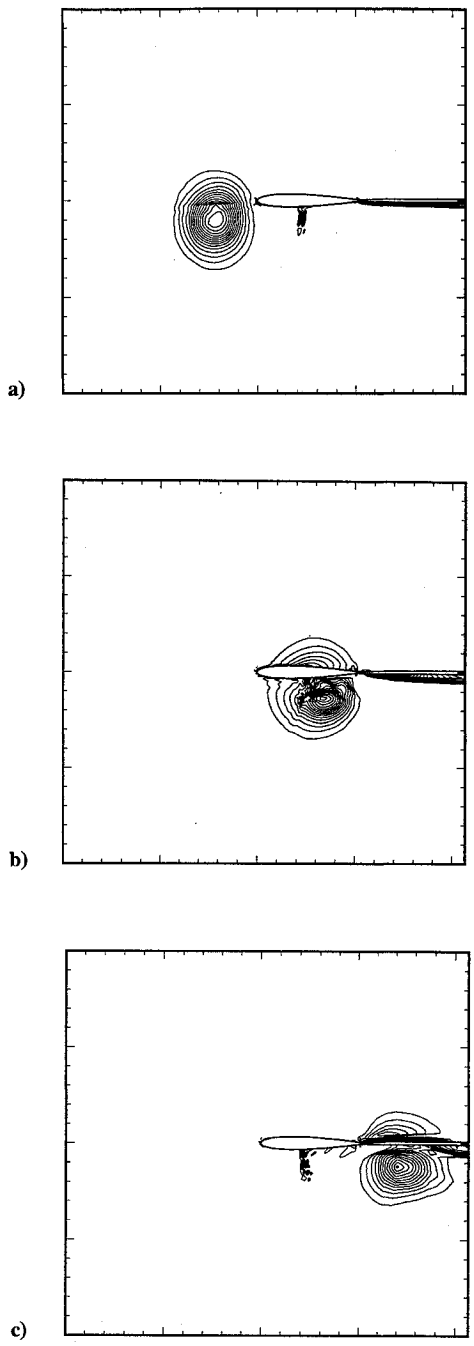

Fig. 5 Instantaneous vortex contours for BVI at time T: a) = 4.4, b) = 5.6, and c) = 6.4.

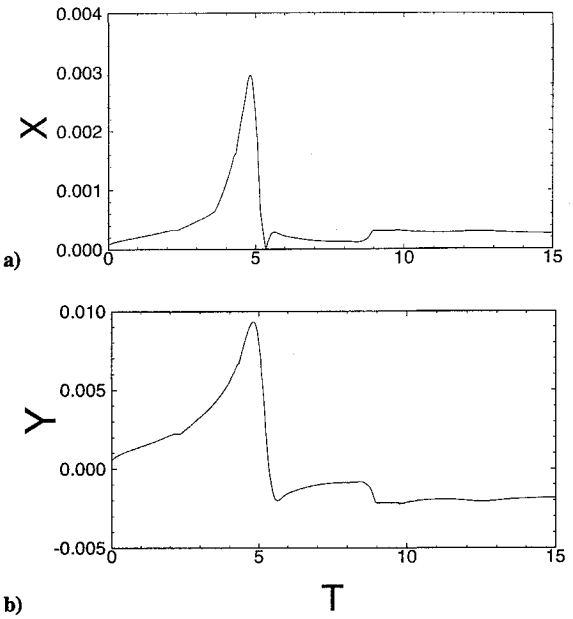

Fig. 6 Stagnation point motion as function of time for a) x coordinate and b) y coordinate.

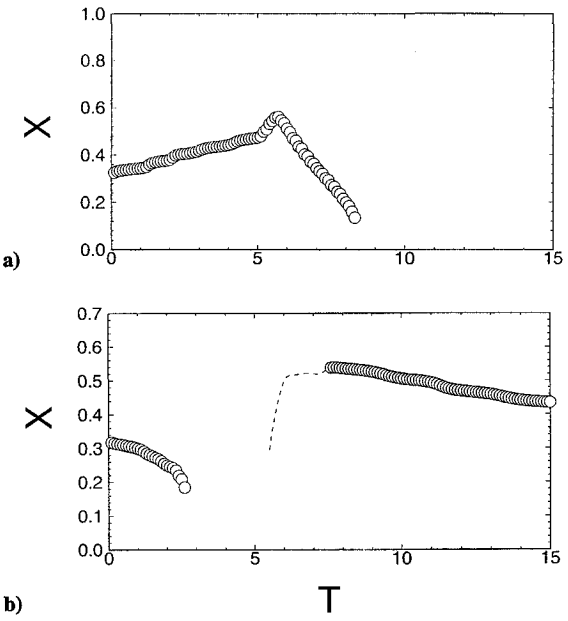

Fig. 7 Shock wave motion on the a) lower surface and b) upper surface.

changing the physical parameters, such as Mach number, vortex strength, and position of vortex, in Sec. VI.

V. Acoustic Wave Analysis

In a linearized analysis of the interaction of a shock wave with a vortex or vortical flow, any small fluctuation can be decomposed into three canonical components,[15] that is, acoustic, entropy, and vorticity waves. The characteristic wave speed of acoustic wave is sound speed, whereas the characteristic wave speed of entropy and vorticity waves is the fluid velocity, so they are also called convective waves. It is well known that any one of the three canonical waves interacting with a shock will generate the other two waves simultaneously.[16,17] However, this linearized decomposition can not be utilized for larger fluctuations. Here, the extraction methods used conform to the analysis of Jou and Menon.[18] Any velocity field $\boldsymbol{u}$ can be separated into two components, a solenoidal field $\boldsymbol{v}$ and a potential field $\nabla\phi$,

$$\boldsymbol{u} = \boldsymbol{v} + \nabla\phi \tag{8}$$

The solenoidal field $\boldsymbol{v}$ satisfies the incompressible condition

$$\nabla \cdot \boldsymbol{v} = 0 \tag{9}$$

and the potential field ϕ includes the dilatation field of $\boldsymbol{u}$ with

$$\nabla^2\phi = \nabla \cdot \boldsymbol{u} = \Delta \tag{10}$$

where Δ is the dilatation field. Since the unsteady fluctuation of the velocity potential is defined as the acoustic disturbances in the flowfield, deducting the time mean averaged dilatation field $\bar{\Delta}$ from its transient total value, the acoustic potential ϕ' can be obtained as

$$\nabla^2\phi' = \Delta - \bar{\Delta} = \Delta' \tag{11}$$

where Δ' (computed by a second-order central difference scheme) is the fluctuation dilatation and can be used to analyze the strength

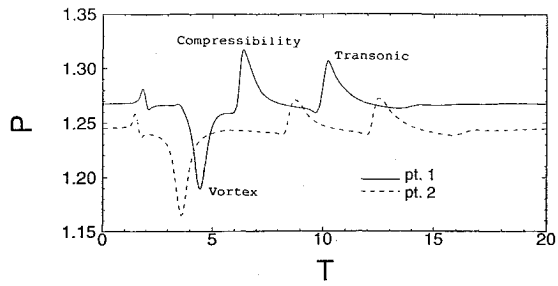

Fig. 8 Pressure history for the observation points ahead the blade.

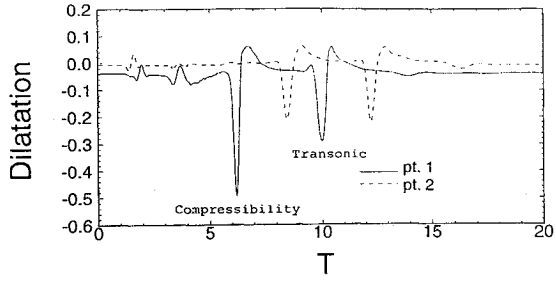

Fig. 9 Dilatation history for the observation points ahead the blade.

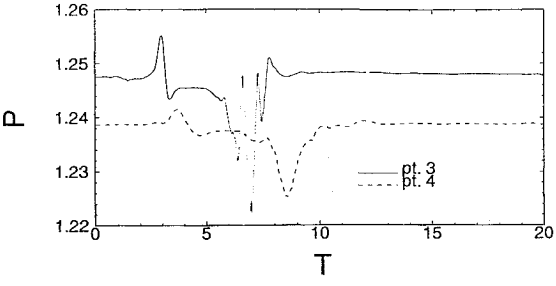

Fig. 10 Pressure history for the second observed group.

of the acoustic disturbances in the blade-vortex interaction. The calculation in Sec. IV was performed up to $t = 15$. The instantaneous dilatation field is analyzed every $\Delta t = 0.02$. The instantaneous fluctuating dilatations are then obtained by subtracting the time averaged values from the instantaneous values.

To realize the propagation direction of the acoustic waves generated in the domain, some test positions were selected, and the transient changes of dilatation and pressure at those points were evaluated. Note that, at each point, the difference between the dilatation and fluctuating dilatation is a constant which may depend on space but not on time. Therefore, at each point, we use the dilatation instead of the fluctuating dilatation to show the fluctuation of the dilatation. The time histories of pressure at points 1 and 2 [$(x, y) = (-0.596, 0.019)$ and $(-1.404, 0.03)$, respectively] are shown in Fig. 8. From those recorded histories, two traveling waves, compressibility and transonic, and the vortex wave, induced by the vortex, are evident. Figure 9 shows the dilatation history at the same points. Again, two traveling waves are evident and the vortex wave as seen in Fig. 8 is not found in this figure. This indicates that, in the near field, using the dilatation field to analyze the acoustic waves is more proper than using the pressure field. The compressibility and transonic wave speeds are found to be $u - c$ approximately, where u is the x-direction velocity component. Thus, these two propagating compression waves due to shock motions are upstream propagating acoustic waves.

The second testing group includes points 3 and 4 [$(x, y) = (2.015, -0.016)$ and $(4.122, -0.0231)$, respectively]. The pressure history of those points are plotted in Fig. 10. Except for the pressure variation due to the passage of the vortex itself, there exists no other obvious traveling wave. From comparison between Figs. 10 and 8, the pressure disturbance propagating downstream is quite small in contrast to pressure disturbances propagating upstream. Therefore, noise is louder ahead of the airfoil than after the airfoil for the transonic BVI flow.

VI. Shock Wave Motion

Lyrintzis et al.[8] has studied the three types A, B, and C of shock motion by using a potential solver. Here, by changing the physical parameters, such as Mach number, vortex strength, and position of vortex, we can also produce these three shock motions in blade-vortex interaction flows.

A. Mach Number $M_\infty = 0.76$: Types B and C

At first, the oncoming freestream Mach number is fixed as 0.76, and the vortex strength Γ is set to be 0.3. We investigate the influence of the vertical distance between the vortex and airfoil by changing the vertical distance from 0.2 to 1.0. The upper and lower surface shock positions are shown in Fig. 11. Because the grid systems adopted are not fine enough to capture the shock sharply, the position where the Mach number is equal to one is defined as the shock position. From Fig. 11, the lower surface shock motion possesses a type-C shock motion, and the upper surface shock motion possesses a type-B shock motion. Moreover, during the approach of the vortex, at the same lateral position, the effect induced by the vortex will be stronger if the vertical distance between the vortex and the airfoil is smaller. Therefore, the lower surface shock with a vertical distance of 0.2 is the quickest one to leave the leading edge, and the shock due to the largest vertical distance of 1.0 is the slowest one to leave the leading edge. Conversely, at the upper surface the strongest shock is obtained if the vertical distance is the shortest. This occurs because the acceleration is larger for a shorter vertical distance at the upper surface.

The effect of the vortex strength is also examined. Theoretically the vortex ought to affect shock motion severely if its strength is strong enough. This is shown in Fig. 12 with freestream Mach number $M_\infty = 0.76$ and initial vortex position $y_0 = -0.2$. When the vortex strength Γ is equal to 0.3, the shock wave has the most intense movement. It moves to the extreme position, which is close to the trailing edge, and it leaves the leading edge the earliest for the cases considered. Also, for the case with $\Gamma = 0.1$, there is a special lower surface shock motion. When the original shock wave moves to approach the leading edge, another compression wave is accumulated to form a new shock at approximately $x = 0.3$.

B. Mach Number $M_\infty = 0.81$: Type A

Now we increase the freestream Mach number to 0.81 and fix the vortex strength Γ to 0.2. Under these conditions both the upper and lower surface shock waves possess the type-A motion as shown in Fig. 13. Since the forces which cause the lower surface shock to move upstream are larger when $y_0 = -0.2$, the shock wave moves upstream quickly. The situation is similar to the case with $M_\infty =$

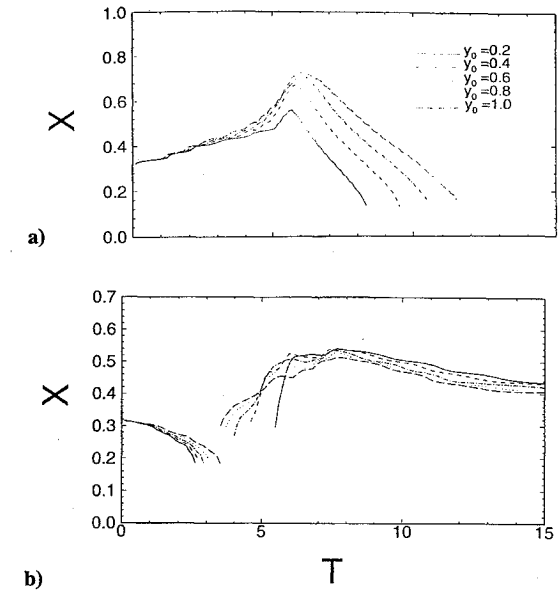

Fig. 11 Shock wave motion, $M_\infty = 0.76$ and $\Gamma = 0.3$, at the a) lower surface and b) upper surface.

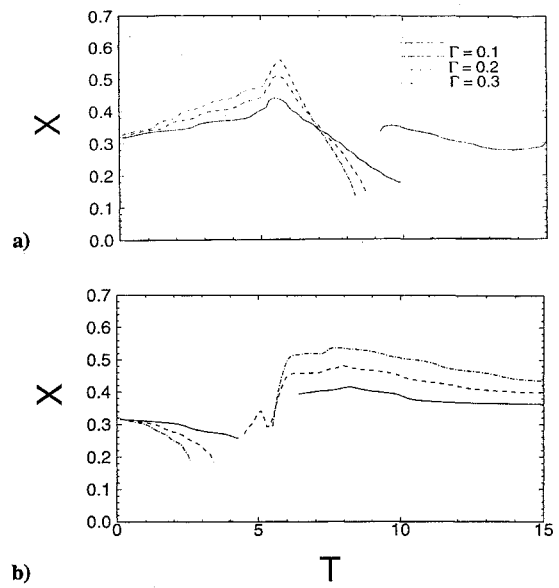

Fig. 12 Shock wave motion, $M_\infty = 0.76$ and $y_0 = -0.2$, at the a) lower surface and b) upper surface.

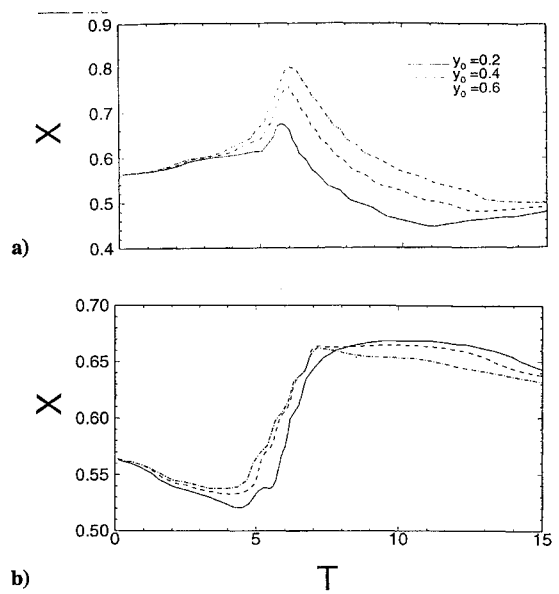

Fig. 13 Shock wave motion, $M_\infty = 0.81$ and $\Gamma = 0.2$, at the a) lower surface and b) upper surface.

0.76 except that there is a type-A shock motion for $M_\infty = 0.81$. We think that this is a type-B shock under this condition rather than type C.

VII. Conclusion

The MOC scheme is applied to study the blade-vortex interaction. Two acoustic waves are observed in this flowfield. They are compressibility and transonic waves. According to the effect induced by the vortex, the stagnation point moves toward the leading edge accompanied by a series of compression waves propagating upstream. These compression waves ultimately merge together to form a shock wave that propagates continuously upstream. This is the compressibility wave. The transonic wave results from the upstream movement of shock that is initially on the lower surface of the blade. The shock moves upstream along the airfoil surface. Finally, it leaves the leading edge and behaves like a compression wave propagating upstream. The acoustic perturbation representation of the dilatation fluctuations shows that the characteristic propagating speed of the two waves is equal to the acoustic propagation speed; these two waves are identified to be acoustic waves. In the future, we will focus our attention on the noise generated by these two waves and attempt to control them. Finally, by changing the physical parameters, such as Mach number, vortex strength, and initial position of the vortex, we have been able to produce the three unsteady shock wave motions, types A, B, and C identified by Tijdeman and Seebass,[4] in blade-vortex interaction flows.

Acknowledgments

This work is partially supported by the National Science Council of the Republic of China. We would like to thank the reviewers and associate editor for giving some valuable suggestions and for correcting our English.

References

[1]Brooks, T. F., and Schlinker, R. H., "Progress in Rotor Broadband Noise Research," *Vertica*, Vol. 7, No. 4, 1983, pp. 287–307.

[2]Schlinker, R. H., and Amiet, R. K., "Rotor-Vortex Interaction Noise," NASA CR 3744, Oct. 1983.

[3]Lent, H. M., Meier, G. E. A., Muller, K. J., Obermeier, F., Schievelbusch, U., and Schurmann, "Mechanisms of Transonic Blade-Vortex Interaction Noise," *Journal of Aircraft*, Vol. 30, No. 1, 1993, pp. 88–93.

[4]Tijdeman, H., and Seebass, R.,"Transonic Flow Past Oscillating Airfoils," *Annual Review of Fluid Mechanics*, 1980, pp. 182–222.

[5]Srinivasan, G. R., McCroskey, W. J., and Baeder, J. D., "Aerodynamics of Two-Dimensional Blade-Vortex Interaction," AIAA Paper 85-1560, July 1985.

[6]George, A. R., and Lyrintzis, A. S., "Acoustics of Transonic Blade-Vortex Interactions," *AIAA Journal*, Vol. 26, No. 7, 1988, pp. 769–776.

[7]Lee, S., Bershader, D., and Rai, M. M., "An Experimental and Computational Study of 2-D Parallel Blade-Vortex Interaction," AIAA Paper 91-3277, Sept. 1991.

[8]Lyrintzis, A. S., Lee, J., and Xue, Y., "Mechanisms and Directivity of Unsteady Transonic Flow Noise," Univ. of Minnesota Supercomputer Institute Research Rept., UMSI 92-25, MN, March 1992.

[9]Lin, S. Y., and Chin, Y. S., "Comparison of Higher Resolution Euler Schemes for Aeroacoustic Computations," *AIAA Journal* (to be published).

[10]Lu, P. J., and Yeh, D. Y., "Transonic Flutter Suppression Using Active Acoustic Excitations," AIAA Paper 93-3285, July 1993.

[11]Roe, P. L., "Approximate Riemann Solvers, Parameter Vectors and Difference Schemes," *Journal of Computational Physics*, Vol. 43, No. 2, 1981, pp. 357–372.

[12]Sculley, M. P., "Computation of Helicopter Rotor Wake Geometry and its Influence on Rotor Harmonic Loads," Aeroelastic and Structure Research Lab., ASRL TR-178-1, Massachussets Inst. of Technology, Cambridge, MA, March 1975.

[13]Yeh, D. Y., "Unsteady Aerodynamic and Aeroelastic Behaviors of Acoustically Excited Transonic Flow," Ph.D. Thesis, National Cheng Kung Univ., Tainan, Taiwan, Republic of China, 1992.

[14]Rai, M. M., "Navier-Stokes Simulations of Blade-Vortex Interaction Using High-Order Accurate Upwind Schemes," AIAA Paper 87-0543, Jan. 1987.

[15]Chu, B.T., and Kovasznay, L. S. G.,"Nonlinear Interaction in a Viscous Heat-Conducting Compressible Gas," *Journal of Fluid Mechanics*, Vol. 3, 1958, pp. 494–514.

[16]Mckenzie, J. F., and Westphal, K. O., "Interaction of Linear Waves with Oblique Shock Waves," *Physics of Fluids*, Vol. 11, No. 11, 1968, pp. 2350–2362.

[17]Zang, T. Z., Hussaini, M. Y., and Dennis, M. B., "Numerical Computations of Turbulence Amplification in Shock-Wave Interaction," *AIAA Journal*, Vol. 22, No. 1, 1984, pp. 13–21.

[18]Jou, W. H., and Menon, S.,"Modes of Oscillation in a Nonreaction Ramjet Combuster Flow," *Journal of Propulsion*, Vol. 6, No. 5, 1990, pp. 535–543.